

Quasiparticle interference patterns as a test for the nature of the pseudogap phase in the cuprate superconductors

T. Pereg-Barnea^{1,2} and M. Franz²

¹ *Kavli Institute for Theoretical Physics, University of California, Santa Barbara, CA 93106-4030*

² *Department of Physics and Astronomy, University of British Columbia, Vancouver, BC, Canada V6T 1Z1*

(Dated: October 24, 2018)

Electrons, when scattered by static random disorder, form standing waves that can be imaged using scanning tunneling microscopy. Such interference patterns, observable by the recently developed technique of Fourier transform scanning tunneling spectroscopy (FT-STs), are shown to carry unique fingerprints characteristic of the electronic order present in a material. We exploit this feature of the FT-STs technique to propose a test for the nature of the enigmatic pseudogap phase in the high- T_c cuprate superconductors. Through their sensitivity to the quasiparticle spectra and coherence factors, the FT-STs patterns in principle carry enough information to unambiguously determine the nature of the condensate responsible for the pseudogap phenomenon. In practice, the absence of a detailed understanding of the scattering mechanism, together with the experimental uncertainties, prevent such an unambiguous determination. We argue, however, that the next generation of FT-STs experiments, currently underway, should be able to distinguish between the pseudogap dominated by the remnants of superconducting order from the pseudogap dominated by some competing order in the particle-hole channel. Using general arguments and detailed numerical calculations, we point to certain fundamental differences between the two scenarios and discuss the prospects for future experiments.

I. INTRODUCTION

The problem of high- T_c superconductivity continues to engage the scientific community, yet much remains unknown. The phase diagram of the cuprates is being elucidated with unprecedented accuracy but a unified microscopic theory of the observed phases is still lacking. While the question of how exactly the Mott-Hubbard antiferromagnetic insulator evolves into a high- T_c superconductor upon hole doping remains unanswered, a number of phenomenological approaches to the problem have been developed. In the absence of a microscopic theory, progress can be made by means of a phenomenological description of the various phases, some of which are motivated by microscopic arguments.^{1,2,3,4,5,6}

Among the various phases, two are especially well established: the antiferromagnet (AF) near the half filling and the superconducting phase which occurs upon hole doping. The latter is reasonably well described by a BCS-like theory with a d -wave symmetric order parameter, $\Delta_{\mathbf{k}}$. It is this symmetry that gives rise to unique physics of the low energy excitations which reside in the vicinity of the nodes of the gap function.

Intermediate between the AF and d -wave superconductor (d SC) is the so called pseudogap phase which exhibits a gap in the single particle density of states but is non-superconducting.⁷ Experimentally, the pseudogap phase is characterized by a d -wave gap in the electron excitation spectrum,⁸ which sets in at a temperature T^* much higher than the superconducting transition temperature T_c . The low energy nodal quasiparticles seem to exist in the pseudogap phase as well, however, they are strongly interacting and exhibit a high scattering rate.⁹

Various authors have made proposals to describe the pseudogap phase using different phenomenological ap-

proaches. One can identify two broad classes of theories. One class includes theories of *competing orders*, in which the pseudogap results from the formation of static or fluctuating order in the particle-hole channel. Examples include the AF spin density wave (SDW), the charge density wave (CDW), stripes, and the so-called d -density wave (DDW, also known as the flux phase). This order parameter is assumed to compete with superconductivity and its formation is energetically favorable in the pseudogap phase.^{4,6,10,11} The other class of theories follow the ideas of *order parameter phase fluctuations*, first introduced by Emery and Kivelson.¹ This school of thought views the pseudogap as a superconductor on short length scales that fails to superconduct on longer length scales due to phase fluctuations. In particular, this implies that a local superconducting order parameter is formed at T^* , but phase coherence is only achieved at T_c .^{1,2,3,5,12,13,14,15} Unraveling the nature of this enigmatic phase is one of the central issues in the physics of high- T_c cuprates.

In this Paper we elaborate on a test for the nature of the pseudogap phase using the Fourier transform scanning tunneling spectroscopy (FT-STs), proposed by us earlier.¹⁶ We demonstrate that the new generation of FT-STs experiments, performed in both the d SC and pseudogap phases, can provide a clear distinction between the two types of order, particle-hole (p-h) or particle-particle (p-p), and can therefore serve as a referee between the above two classes of theories. Such a distinction is possible due to fundamental differences between the two types of order. In a superconductor the elementary excitations consist of an admixture of electrons and holes. The charge of these quasiparticles is not a good quantum number, and each quasiparticle carries a quantum phase that describes its particle-hole mixing. As a result, scattering processes which give rise to the FT-

STS signal, have high or low probability depending on the relative phase of the scattering quasiparticles. This probability is given by the relevant *coherence factors*. On the other hand, when the scattering amplitude may depend on various microscopic details, we show that there exist certain generic features which only depend on the type of ordering present in the system.

The most straightforward test follows from the following simple consideration. The interference patterns caused by a p-p order parameter are known; these are just the experimental results observed in cuprates below T_c .^{17,18} Comparing these patterns with the experimental results in the pseudogap phase should reveal the nature of the pseudogap order parameter. If the patterns are similar to those of the *d*SC state, it is likely that the pseudogap order is in the p-p channel. If, on the other hand, an abrupt change in the patterns is found, the conclusion will be that a different type of order, in the p-h channel, governs the pseudogap. We shall discuss the relation to the available experimental data in Sec. IV.C.

This article is organized as follows. In the next section we revisit the formalism of the quasiparticle interference in the superconducting state, reviewing some recent theoretical work and commenting on the agreement with experiment. We choose a framework for further analysis and discuss how it may be justified on microscopic grounds. In section III we apply the same theoretical treatment to the pseudogap phase. We give a general discussion of the problem and then study two representative theories of the pseudogap, the QED₃ theory and *d*-density wave (DDW). We comment on their relevance in light of experimental observations. Our conclusions are given in section IV.

II. THE SUPERCONDUCTING STATE

A. General considerations

In the high resolution FT-STs experiments the spectrometer's sharp tip is placed above a freshly cleaved sample surface, and a bias voltage is applied between the sample and tip. Tunneling occurs through the vacuum barrier and produces electric current which is measured as a function of the bias voltage. The measured differential conductance $dI(V, \mathbf{r})/dV$ is proportional to the local density of states (LDOS) $n(\mathbf{r}, \omega)$ of the sample below the STS tip at the point \mathbf{r} . A wide field of view of about $600\text{\AA} \times 600\text{\AA}$ is scanned with atomic resolution, and at each bias voltage the spatial map of $n(\mathbf{r}, \omega)$ is collected. The spatial Fourier transform of this quantity, $n(\mathbf{k}, \omega)$, is then studied. The resulting *k*-space distribution^{17,18,19} reveals distinctive patterns with peaks at special wave vectors that correspond to certain periodic structures in the real space electron wavefunctions. In a clean, homogeneous superconductor such structures would be absent; they apparently result from the translational symmetry breaking caused by disorder. At present, the details of

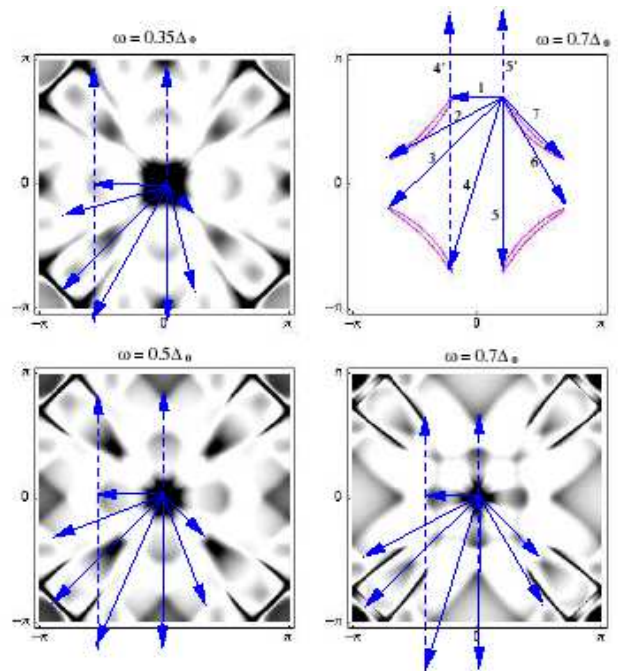


FIG. 1: Top right: The banana shape contours of constant low energy around the nodes of the gap and seven vectors connecting their ends at energy $\omega = 0.7\Delta_0$.¹⁷ Top left and bottom: Numerical evaluation of the Fourier transformed local density of states in Eq. (12) with $t' = 0.3t$, $\Delta_0 = 0.2t$, $\mu = -t$ and $\omega = 0.35, 0.5$ and $0.7\Delta_0$ respectively. In order to best fit the experimental data^{17,18} we present the real part of $\Lambda(q, \omega)$ and suppress the $\Delta_+ \Delta_-$ term as explained in the text.

this scattering potential are not fully understood.

These pioneering FT-STs experiments were followed by several theoretical studies that calculated the LDOS modulations in the BCS *d*-wave model using various approximations.^{16,20,21,22} First, a heuristic picture referred to as the *octet model* was put forward by Hoffman *et al.*^{17,18,20} and provided a simple and appealing explanation of the data. The octet model identifies eight points in momentum space at which there is the largest single particle density of states (DOS), and asserts that the experimental FT LDOS is expected to have a peak at any point \mathbf{q} in the Brillouin zone such that \mathbf{q} connects any two of the octet points. As illustrated in Fig. 1 the latter occurs at the ends of the banana shaped contours of constant energy (CCE), where the energy is equal to the bias voltage, $\hbar\omega = eV$.

The original octet model explains the experimental data surprisingly well, considering that it ignores several important issues. In particular, the on-shell excitations away from the octet points are not taken into account. One can argue that such excitations have lower single-particle DOS than the octet model points. However, the ratio between the single particle DOS at the edges of the CCE bananas to the DOS of any other point on the CCE is only a result of the velocity anisotropy and is not as

significant as other considerations. This can be seen by expanding the energy dispersion near the nodes and calculating the DOS. In the “nodal” approximation, scaling the momentum coordinates by the appropriate velocities (v_F and v_Δ) leads to a circular CCE, on which there is no special point that could define a peak position.

A more detailed analysis compares the measured spectrum to a joint density of states (JDOS), $D(\mathbf{q}, \omega)$, given by a \mathbf{k} -space convolution of the single particle density of states

$$D(\mathbf{q}, \omega) = \sum_{\mathbf{k}} \delta(\omega - E_{\mathbf{k}}) \delta(\omega - E_{\mathbf{k}-\mathbf{q}}), \quad (1)$$

where $E_{\mathbf{k}}$ is the single particle excitation energy in the superconductor. This approach includes the on-shell processes away from the nodal points but neglects the off-shell processes as well as the coherence factors. We shall see shortly that in a d -wave superconductor the coherence factors for scalar disorder are precisely such as to greatly enhance the contributions from the octet points. We also find that the off-shell processes mostly contribute to the background and, interestingly, tend to worsen the agreement with experimental data.

It is interesting to note that the theoretically more satisfying approaches^{16,20,21,22}, which model the LDOS using the full electron Green’s function (computed within various reasonable approximations), generally fail to account for the details of the experimentally observed patterns. The main problem is that these theoretical approaches typically produce a number of prominent background features that are not present in experiment. As a result, the computed patterns do not really resemble the experimental data (compare, e.g., Refs. 20 and 18), even if they contain many of their characteristic features. At present it is not clear whether this discrepancy is a sign of some fundamental difficulty in the existing models or simply a question of details that have not been yet properly addressed.

Here we take the latter view; i.e. that a simple BCS-type model of a d -wave superconductor with appropriate disorder should provide a complete description of the FT-STS data once the details of the scattering mechanism have been ironed out. In the present paper we are interested in these details only to the extent that will allow us to establish a baseline for our discussion of FT-STS in the *pseudogap* state. With this goal in mind in what follows we design a model for scattering in the d SC that produces patterns in reasonable agreement with the experiment. We also explore several routes to justify this model from microscopic considerations, but in this we are only partially successful. We then take this same model and use it to discuss the pseudogap state.

B. The model

We shall describe the system by a standard BCS d -wave Hamiltonian with disorder, treated as a perturba-

tion. In the following, we consider three types of disorder, namely in the charge, spin and pairing channels. We show how different types of disorder produce different scattering patterns and comment on their relation to the patterns observed in the FT-STS experiments. Our starting point is similar to that used by previous authors^{20,21,22} but there will be some differences which will allow us to closely reproduce the experimental data.

The system is described by the Hamiltonian $\mathcal{H} = \mathcal{H}_0 + \delta\mathcal{H}$, where

$$\mathcal{H}_0 = \sum_{\mathbf{k}} \psi_{\mathbf{k}}^\dagger \begin{pmatrix} \epsilon_{\mathbf{k}} & \Delta_{\mathbf{k}} \\ \Delta_{\mathbf{k}}^* & -\epsilon_{\mathbf{k}} \end{pmatrix} \psi_{\mathbf{k}}$$

is the d -wave BCS Hamiltonian describing the pure, uniform d SC. $\psi_{\mathbf{k}}^\dagger = (c_{\mathbf{k}\uparrow}^\dagger, c_{-\mathbf{k}\downarrow})$ is the Nambu space creation operator and $\epsilon_{\mathbf{k}}$, $\Delta_{\mathbf{k}}$ are the band structure and gap function respectively. In what follows, we choose to work with the second-nearest neighbor hopping model and a $d_{x^2-y^2}$ gap function

$$\begin{aligned} \epsilon_{\mathbf{k}} &= -2t(\cos k_x + \cos k_y) - 4t' \cos k_x \cos k_y - \mu, \\ \Delta_{\mathbf{k}} &= \frac{1}{2} \Delta_0 (\cos k_x - \cos k_y). \end{aligned} \quad (2)$$

Disorder is generically described by a Hamiltonian

$$\delta\mathcal{H} = \sum_{i,j,\sigma,\sigma'} V_{ij}^{\sigma\sigma'} c_{i\sigma}^\dagger c_{j\sigma'} = \sum_{\mathbf{k},\mathbf{k}'} \psi_{\mathbf{k}}^\dagger \hat{V}_{\mathbf{k}\mathbf{k}'} \psi_{\mathbf{k}'}. \quad (3)$$

Here i, j is a lattice index, $V_{ij}^{\sigma\sigma'}$ is the random potential and $\hat{V}_{\mathbf{k}\mathbf{k}'}$ its Fourier transform, a 2×2 matrix in Nambu space.

The electron propagator of the perturbed system can be expressed as

$$G(\mathbf{k}, \mathbf{k}', \omega) = G^0(\mathbf{k}, \omega) \delta_{\mathbf{k},\mathbf{k}'} + G^0(\mathbf{k}, \omega) \hat{T}_{\mathbf{k}\mathbf{k}'}(\omega) G^0(\mathbf{k}', \omega), \quad (4)$$

where

$$G^0(\mathbf{k}, \omega) = [\omega - \sigma_3 \epsilon_{\mathbf{k}} - \sigma_1 \Delta_{\mathbf{k}}]^{-1} \quad (5)$$

is the bare Green’s function and σ_i are the Pauli matrices. $\hat{T}_{\mathbf{k}\mathbf{k}'}(\omega)$ is the T -matrix, subject to the Lippman-Schwinger equation

$$\hat{T}_{\mathbf{k}\mathbf{k}'}(\omega) = \hat{V}_{\mathbf{k}\mathbf{k}'} + \sum_{\mathbf{q}} \hat{V}_{\mathbf{k}\mathbf{q}} G^0(\mathbf{q}, \omega) \hat{T}_{\mathbf{q}\mathbf{k}'}(\omega). \quad (6)$$

The local density of states at the point \mathbf{r} of the sample is then given by

$$n(\mathbf{r}, \omega) = -\frac{1}{\pi} \text{Im}[G_{11}(\mathbf{r}, \mathbf{r}, \omega) + G_{22}(\mathbf{r}, \mathbf{r}, -\omega)], \quad (7)$$

where $G(\mathbf{r}, \mathbf{r}', \omega)$ is the spatial Fourier transform of $G(\mathbf{k}, \mathbf{k}', \omega)$. Here and hereafter “Im” is understood as taking the usual difference between the retarded and the advanced quantity measuring the discontinuity of the

propagator across the real frequency axis. It is important to keep this in mind since $\hat{V}_{\mathbf{k}\mathbf{k}'}$ is in general complex but its imaginary part does *not* contribute to the above discontinuity and therefore to LDOS in Eq. (7). Taking the “Im” symbol literally would lead to incorrect results.

For arbitrary disorder one must typically solve for the T -matrix from Eq. (6) using numerical methods. We shall not attempt such a detailed numerical solution here. Rather, we shall limit ourselves to two different approximations where progress can be made analytically. First, we consider the limit of *weak* but otherwise arbitrary disorder. Second, we study the case of arbitrarily strong but *dilute* point-like scatterers.

C. Weak scattering (Born limit)

To leading order in the scattering potential V , i.e., in the Born approximation, we have $\hat{T}_{\mathbf{k}\mathbf{k}'}(\omega) \simeq \hat{V}_{\mathbf{k}\mathbf{k}'}$ and the perturbed Green’s function is given by

$$G(\mathbf{k}, \mathbf{k}', \omega) = G^0(\mathbf{k}, \omega)\delta_{\mathbf{k}, \mathbf{k}'} + G^0(\mathbf{k}, \omega)\hat{V}_{\mathbf{k}\mathbf{k}'}G^0(\mathbf{k}', \omega). \quad (8)$$

Since the first term of Eq. (8) is uniform, all the interesting information resides in the second term.

We now focus on the disorder potential in the *charge* channel. In this case we have on-site random potential V_i coupled to electron charge,

$$\delta\mathcal{H} = \sum_{i,\sigma} V_i c_{i\sigma}^\dagger c_{i\sigma} = \sum_{\mathbf{k}, \mathbf{k}'} V_{\mathbf{k}-\mathbf{k}'} \psi_{\mathbf{k}}^\dagger \sigma_3 \psi_{\mathbf{k}'} \quad (9)$$

i.e., $\hat{V}_{\mathbf{k}\mathbf{k}'} = \sigma_3 V_{\mathbf{q}}$, where $V_{\mathbf{q}}$ is the Fourier transform of V_i . The advantage of the Born limit is that one may express the interesting non-uniform part of the measured FT LDOS, $\delta n(\mathbf{q}, \omega)$, in a factorized form²¹

$$\delta n(\mathbf{q}, \omega) = -\frac{1}{\pi} |V_{\mathbf{q}}| \text{Im} [\Lambda_{11}(\mathbf{q}, \omega) + \Lambda_{22}(\mathbf{q}, -\omega)], \quad (10)$$

where

$$\Lambda(\mathbf{q}, \omega) = \sum_{\mathbf{k}} G^0(\mathbf{k}, \omega) \sigma_3 G^0(\mathbf{k} - \mathbf{q}, \omega). \quad (11)$$

As discussed by Capriotti *et al.* $V_{\mathbf{q}}$ is a random function with no interesting structure while $\Lambda(\mathbf{q}, \omega)$ contains information about the underlying clean system. Any peaks observed in $\delta n(\mathbf{q}, \omega)$ therefore must be attributed to $\Lambda(\mathbf{q}, \omega)$. Thus, by studying the interference patterns in a disordered sample one can learn about the properties of the system in the absence of disorder.

With the d -wave BCS Green’s function, Eq. (5), one finds

$$\Lambda_{11}(\mathbf{q}, i\omega) = \frac{1}{L^2} \sum_{\mathbf{k}} \frac{(i\omega + \epsilon_+)(i\omega + \epsilon_-) - \Delta_+ \Delta_-}{(\omega^2 + E_+^2)(\omega^2 + E_-^2)}, \quad (12)$$

with $\epsilon_{\pm} = \epsilon_{\mathbf{k} \pm \mathbf{q}/2}$, $\Delta_{\pm} = \Delta_{\mathbf{k} \pm \mathbf{q}/2}$ and $E_{\pm} = \sqrt{\epsilon_{\pm}^2 + \Delta_{\pm}^2}$. Eq. (12) can be evaluated exactly using numerical methods. However, before doing so we shall elucidate its main

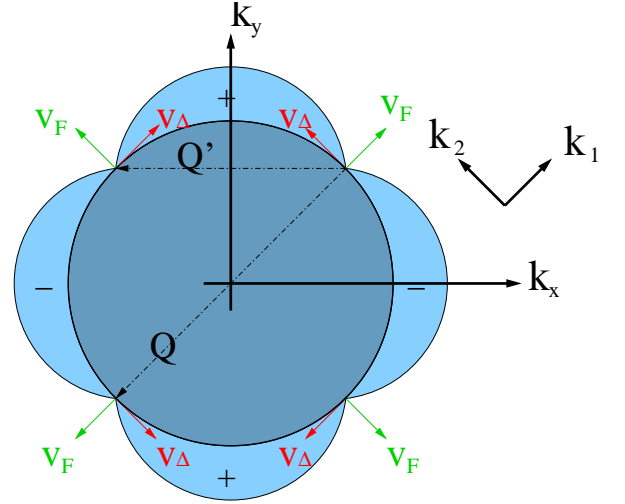


FIG. 2: The nodes of the d SC gap on the underlying Fermi surface with the velocities v_F and v_{Δ} as defined in each node. The vectors \mathbf{Q} and \mathbf{Q}' span antipodal and adjacent nodes respectively.

features by employing the nodal approximation. In this approximation, valid at energies low compared to the maximum gap Δ_0 , the spectrum is linearized in the vicinity of the nodes, and we consider scattering processes either within the same node or between different nodes. Let us first evaluate the LDOS resulting from intra-node scattering, which corresponds to the octet vector \mathbf{q}_7 .¹⁸ For this case, Eq. (12) can be approximated in the following way: near the node we use the 45° rotated coordinates k_1 and k_2 shown in Fig. (2). To first order in the momentum we expand $\epsilon_{\mathbf{k}} \rightarrow v_F k_1$ and $\Delta_{\mathbf{k}} \rightarrow v_{\Delta} k_2$. We then rescale the momentum coordinates so that $v_F k_1 \rightarrow k_1$, $v_{\Delta} k_2 \rightarrow k_2$, and redefine $\frac{1}{2} v_F q_1 \rightarrow \tilde{q}_1$ and $\frac{1}{2} v_{\Delta} q_2 \rightarrow \tilde{q}_2$. In the scaled coordinate frame $E_{\mathbf{k}} = |\mathbf{k}|$ and Eq. (12) simplifies to

$$\Lambda_{\text{lin}} = \frac{1}{v_F v_{\Delta}} \int \frac{d^2 k}{(2\pi)^2} \frac{-\omega^2 + (k_1^2 - k_2^2) - (\tilde{q}_1^2 - \tilde{q}_2^2)}{[\omega^2 + (\mathbf{k} + \tilde{\mathbf{q}})^2][\omega^2 + (\mathbf{k} - \tilde{\mathbf{q}})^2]}. \quad (13)$$

As shown in appendix A, the explicit solution can be found using the Feynman parameterization²⁸ and reads:

$$\Lambda_{\text{lin}}(\mathbf{q}, \omega) = \frac{1}{2\pi v_F v_{\Delta}} \left[\left(\frac{\tilde{q}_2}{\tilde{q}} \right)^2 \mathcal{F} \left(\frac{\omega}{\tilde{q}} \right) - \frac{1}{2} \right], \quad (14)$$

$$\mathcal{F}(z) = 1 - \frac{z^2}{\sqrt{z^2 - 1}} \arctan \frac{1}{\sqrt{z^2 - 1}}.$$

The function $\mathcal{F}(z)$ implies an inverse square root singularity in both the real and imaginary parts of $\Lambda_{\text{lin}}(\mathbf{q}, \omega)$ along an elliptic contour of constant energy given by $E_{\mathbf{q}} = 2\omega$ (here $E_{\mathbf{q}} = 2\tilde{q} \equiv \sqrt{v_F^2 q_1^2 + v_{\Delta}^2 q_2^2}$). More importantly, this singularity is weighted by an angular factor $(\tilde{q}_2/\tilde{q})^2 = (v_{\Delta} q_2/E_{\mathbf{q}})^2$, producing the largest amplitude at the two ends of the ellipse, as illustrated in Fig. (3a). These points of largest intensity coincide with $\pm \mathbf{q}_7$. It

is important to note that the angular dependence results purely from the coherence factors (i.e. terms in the numerator of Eq. 13) and would not appear in the JDOS Eq. (1).

This particular angular dependence can be understood by analyzing the relevant BCS coherence factors as follows. Consider first \mathbf{q} that connects the two CCE point along the nodal direction. The process represents scattering of a pure particle to a pure hole since along this direction there is no p-h mixing due to the vanishing gap. The amplitude of such a process is zero due to the charge coupling. On the other hand the two points at the edges of the CCE both have equal particle and hole mixing ($|u_{\mathbf{k}}| = |v_{\mathbf{k}}|$ in the BCS notation) and the same quantum phase. This leads to constructive interference and maximal $\Lambda(\mathbf{q}, \omega)$.

Similarly, we can treat magnetic disorder. In this case, the potential couples to the electron spin and is therefore proportional to the unit matrix $\sigma_0 = \mathbb{1}$ in Nambu space:

$$\delta\mathcal{H} = \sum_i V_i^{\text{mag}} [c_{i\uparrow}^\dagger c_{i\uparrow} - c_{i\downarrow}^\dagger c_{i\downarrow}] = \sum_{\mathbf{k}, \mathbf{k}'} V_{\mathbf{k}-\mathbf{k}'}^{\text{mag}} \psi_{\mathbf{k}}^\dagger \sigma_0 \psi_{\mathbf{k}'}. \quad (15)$$

Again, one can describe the scattering patterns using $\Lambda(\mathbf{q}, \omega)$. It is easy to see that the expression for this quantity is just like Eq. (12) except for the sign change in front of the $\Delta_+ \Delta_-$ term. In the nodal approximation for intra-nodal scattering we thus get

$$\Lambda_{\text{lin}}^{\text{mag}} = \frac{1}{v_F v_\Delta} \int \frac{d^2 k}{(2\pi)^2} \frac{-\omega^2 + \mathbf{k}^2 - \tilde{\mathbf{q}}^2}{[\omega^2 + (\mathbf{k} + \tilde{\mathbf{q}})^2][\omega^2 + (\mathbf{k} - \tilde{\mathbf{q}})^2]}. \quad (16)$$

The solution (see Appendix A) is now very different,

$$\Lambda_{\text{lin}}^{\text{mag}}(\mathbf{q}, \omega) = \frac{-1}{2\pi v_F v_\Delta} \left[i\pi + 2\mathcal{F}'\left(\frac{\omega}{\tilde{q}}\right) + \ln\left(\frac{\omega^2}{\lambda^2}\right) \right],$$

$$\mathcal{F}'(z) = \sqrt{z^2 - 1} \arctan \frac{1}{\sqrt{z^2 - 1}}. \quad (17)$$

Here, since the spin is a good quantum number, no angular dependent coherence factors are present, and the interference amplitude is constant along the elliptic contour $2\omega = \sqrt{v_F^2 q_1^2 + v_\Delta^2 q_2^2}$, as shown in Fig. (3d). The square root singularity is replaced by a cusp along the contour. This result provides another example of the importance of the coherence factors.

The linearized treatment for internodal magnetic and non-magnetic scattering is similar and given in appendix A. A composite picture including scattering processes between all nodes is shown in panel (e) of Fig. (3). We observe that it indeed contains peaks and qualitatively exhibits features observed in FT-STs experiments. The linearized treatment also indicates that non-magnetic scattering alone cannot produce all of the experimentally observed features. The octet points \mathbf{q}_1 , \mathbf{q}_5 and $\mathbf{q}_{2,6}$, corresponding to adjacent nodes scattering, can all be produced together only by including magnetic scattering (see Fig. (3c)). This combination of magnetic

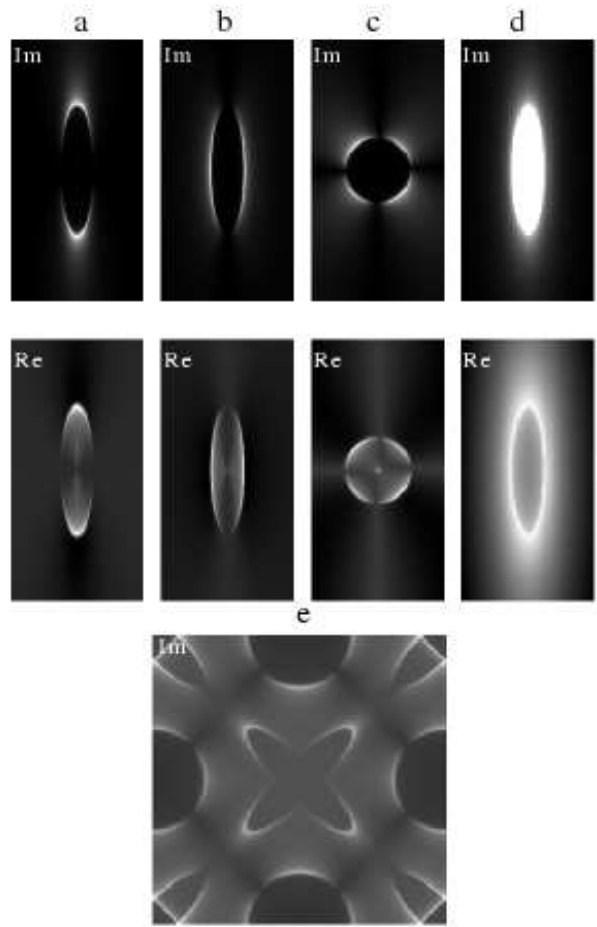


FIG. 3: Interference patterns in the nodal approximation. a) Non-magnetic scattering within a single node Eq. (8), b) Non-magnetic scattering between two antipodal nodes, Eq. (A4), c) Magnetic scattering between adjacent nodes, Eq. (A5), d) Magnetic scattering within a single node, or antipodal nodes and non magnetic scattering of adjacent nodes. In (a,b,d) we used $v_F/v_\Delta = 4$ and in (c) $v_F/v_\Delta = 1$. Note that the axes here represent the nodal coordinates, q_1 (horizontal) and q_2 . e) A composite of the intra- and antipodal-node terms for non-magnetic scattering and adjacent-node magnetic scattering showing the full Brillouin zone distribution in the nodal approximation.

and non-magnetic scattering is discussed in the next subsection.

Beyond the linearized approximation, the interference patterns can be evaluated exactly, by numerical methods, using the full model dispersion Eq. (2). Work along these lines has been done for a single point like scatterer in Refs. 20,21,22 and for arbitrary weak disorder in Refs. 21,23. To evaluate Eq. (12) numerically we find it convenient to perform the momentum space Green's function convolutions by employing the fast Fourier transform (FFT) technique. In particular we transform $G^0(\mathbf{k}, \omega)$ to real space, multiply the appropriate components, and perform an inverse FFT back to the momentum space.

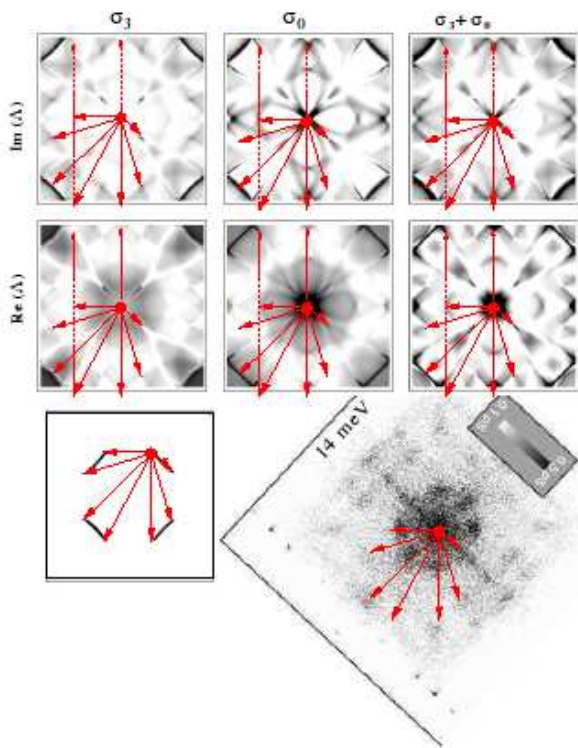


FIG. 4: Top six panels: numerical evaluation of $\Lambda(\mathbf{q}, \omega)$ for $\omega = 0.32\Delta_0$, where the scattering potential is, from left to right proportional to σ_3 (non-magnetic scattering), $\sigma_0 = \mathbb{1}$ (magnetic scattering) and an equal combination of both. Bottom: The octet points at the edges of the banana shaped CCE (left) and the experimental data of $14\text{meV} \approx 0.32\Delta_0$ from Ref. 18 (right). Note that the Brillouin zone of the experimental data is 45° rotated with respect to the crystallographic directions.

Since the run time of FFT is only $o(n \log(n))$ where n is the array size, this allows for fast evaluation of $\Lambda(\mathbf{q}, \omega)$ on large lattices (of up to 1024×1024 lattice points).

The comparison of numerical results with the experimental data shown in Fig. (4) leads to two interesting insights. When considering the Born limit of point-like charge/spin impurities represented by σ_3 or σ_0 matrices respectively, it appears that the real rather than the imaginary part of $\Lambda(\mathbf{q}, \omega)$ is describing the experiment more accurately. In addition, one achieves even better agreement with the data when neglecting the off-diagonal part of the unperturbed Green's function [i.e. $\Delta_+\Delta_-$ term in Eq. (12)]. Operationally, such suppression of the off diagonal Green's function may be achieved as a result of an even combination of magnetic and non-magnetic scattering since the two contain contributions proportional to $\Delta_+\Delta_-$ with opposite signs. Fig. (4) shows our numerical calculation of $\Lambda(\mathbf{q}, \omega)$ for a magnetic, non-magnetic and an even combination of both types of scattering. Our best fit to the data is obtained by taking the *real* part of the equal mixture of magnetic and non-magnetic scattering and is presented in Fig. (1).

We adopt this result for FT-STs in *dSC* as our baseline for studies of the pseudogap state. Before we proceed to study the latter we briefly discuss how one could justify this model based on the physics beyond the Born approximation.

D. Beyond the Born limit: the T -matrix

As mentioned above, the Born limit scattering model is in best agreement with the experimental data when (i) the off-diagonal part of the bare Green's function, $\mathcal{F}(\mathbf{k}, i\omega) = \Delta_{\mathbf{k}}/(\omega^2 + E_{\mathbf{k}}^2)$, is ignored and (ii) the real part of Λ rather than the imaginary part is taken (in contrast to the prescription in Eq. (10)). The question naturally arises: can this prescription be justified in a physically well motivated manner?

(i) may arise simply as a result of chemistry; it is in principle possible that impurities in cuprates act both as charge and spin scatterers and that the strength in both channels is roughly equal. However, such an assumption amounts to a fine tuning of parameters. Furthermore, chemistry cannot plausibly explain (ii).

We now show that at least qualitatively both effects may arise when the disorder potential is not weak and the full T -matrix is considered. In the T -matrix, all of the terms in the Born series are resummed by means of Eq. (6). Unfortunately, solving the Lippman-Schwinger equation for arbitrary disorder potential is a daunting task. Progress can be made, however, in the case of point-like scatterers. In particular, for a single point-like scatterer at the origin, the T -matrix becomes momentum independent and its ω dependence can be found analytically.²⁴ One can easily see that the expression for $\delta n(\mathbf{q}, \omega)$ must be modified as

$$\delta n(\mathbf{q}, \omega) = -\frac{1}{\pi} \text{Im} \sum_{\mathbf{k}} G^0(\mathbf{k}, \omega) \hat{T}(\omega) G^0(\mathbf{k} - \mathbf{q}, \omega). \quad (18)$$

In the following, we focus on this analytically tractable situation which is also relevant to a dilute concentration of point scatterers provided that one can neglect coherent scattering from multiple impurities.

First note that in a superconductor, a charge scatterer, which is represented by a potential proportional to σ_3 in Nambu space, generates terms proportional to σ_0 in the Born series. These terms are *magnetic-like* since the magnetic potential is represented by a unit matrix. Magnetic-like terms arise from a pure charge impurity due to the 2×2 structure of the Green's function (there is no symmetry that forbids their creation). Second, the T -matrix is in general complex. Thus, there could be a regime in which its imaginary part dominates, implying that $\delta n(\mathbf{q}, \omega)$ would receive dominant contributions from the real part of $\Lambda(\mathbf{q}, \omega)$.

As shown by Balatsky *et al.*,²⁴ near half filling summing the Born series for the point-like charge impurity

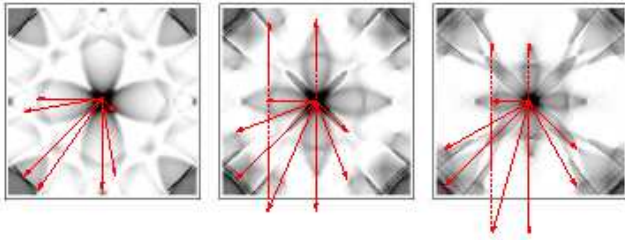


FIG. 5: The T -matrix approximation for a point like charge impurity and a local gap modulation at the origin. The band structure parameters and gap magnitude are the same as in Fig. (1) and $V = 0.3t$, $\delta\Delta = 0.3\Delta_0$. The frequencies from left to right are $0.2, 0.5$ and $0.7\Delta_0$.

yields $\hat{T}(\omega) = T_0(\omega)\sigma_0 + T_3(\omega)\sigma_3$ with

$$T_0(\omega) = \frac{g_0(\omega)}{c^2 - g_0^2(\omega)}, \quad T_3(\omega) = \frac{-c}{c^2 - g_0^2(\omega)} \quad (19)$$

where $c = \cot \delta_0$ is the cotangent of the scattering phase shift and $g_0(\omega) = \text{Tr} \sum_{\mathbf{k}} G^0(\mathbf{k}, \omega)$. The above frequency structure of the T -matrix represents a quasi-bound state near the impurity with a resonance at $c = \pm g_0(\omega)$. Since c is a real number and the Green's function has an imaginary part, at resonance the T -matrix is predominantly imaginary and $T_3(\omega) \approx \mp T_0(\omega)$. This means that near resonance both (i) and (ii) can be satisfied and the prescription that we obtained heuristically in the previous subsection can be physically motivated.

Our justification above should be viewed merely as a “proof of principle” since the arguments only hold near the resonant frequency whereas we need them to apply at all frequencies. One could perhaps argue that in real samples the impurity resonances will be distributed forming a continuous band in which $\hat{T}(\omega)$ is predominantly imaginary and $T_3(\omega) \approx T_0(\omega)$. However at this stage this is merely a speculation.

Another mechanism that can give rise to suppression of the off-diagonal terms is spatial variation of the gap amplitude. Such variations have indeed been observed in the STS studies on BiSCCO samples.^{25,26} Theoretical treatment of these is somewhat complicated by the fact that in a d SC the order parameter lives on the nearest neighbor bonds of the underlying ionic lattice. For that reason we defer this discussion to the Appendix B.

Our numerical results for a point-like impurity (including the gap suppression) in the T -matrix approximation at the relevant probing frequencies are presented in Fig. 5. The obtained results are similar to those obtained by the simple treatment of section IIC (Fig. 1) and display most of the features expected by the octet model. We emphasize again that considerations in this subsection are not meant as detailed modeling of the scattering potentials in the cuprates. Rather, they are meant to illustrate how the heuristic treatment presented in the previous subsection can be reconciled with a more microscopic approach. In what follows we shall continue

to describe the FT-STs patterns $\delta n(\mathbf{q}, \omega)$ in terms of $\Lambda(\mathbf{q}, \omega)$ via Eq. (10).

III. THE PSEUDOGAP STATE

We now focus on the pseudogap state. In principle, the information contained in the FT-STs patterns should permit the unambiguous determination of the electron order present in underdoped cuprates above T_c (but below T^*). In practice, however, we have seen that details of the scattering mechanism can lead to vastly different interference patterns, and even the description of the well-understood d SC state is fraught with difficulty. We thus set our sights on a more modest goal; in the following we consider the question whether it is possible, using the FT-STs techniques, to identify the condensate in the pseudogap state as being in the p-p (superconducting) or p-h channel.

As we have seen above the p-p order in the superconducting phase gives rise to very special BCS coherence factors which mix electron and hole degrees of freedom. These coherence factors lead to unique FT-STs patterns with sharp peaks at the set of “octet vectors” shown in Fig. (1). According to our analysis there are two crucial factors which determine the position of these peaks in the Brillouin zone. The quasiparticle *excitation spectrum* $E_{\mathbf{q}}$ defines a set of contours of constant energy, $E_{\mathbf{q}} = \pm\omega$, along which the denominators of Eq. (12) vanish and cause large FT-STs response. The *coherence factors*, entering the numerator of Eq. (12), determine whether the quasiparticle interference is constructive or destructive at a given point and thus select special points along these contours at which the peaks in FT-STs appear.

It follows from this analysis that the observed FT-STs patterns will change when either the excitation spectrum *or* the coherence factors are modified as one passes from d SC to the pseudogap state. This observation is the key to our proposal to distinguish between the pairing and p-h correlations in the pseudogap state. If, on crossing the T_c , the FT-STs patterns are essentially unmodified, then one can conclude that the pseudogap is dominated by ordering in the p-p channel. If, on the other hand, a qualitatively different pattern is observed above T_c , then this would be evidence for another type of order, most likely in the p-h channel. These conclusions should be insensitive to the details of the scattering mechanism that give rise to the quasiparticle interference.

A more complicated situation may arise when the competing order can coexist with superconductivity in some region of the phase diagram, as envisioned e.g. in Ref. 6. In that case the above analysis still applies but one expects a more gradual change of the interference patterns as a function of temperature (or another control parameter such as doping) reflecting the gradual growth of the competing order at the expense of superconductivity.

In order to illustrate the crucial role the type of order

parameter plays in the process of quasiparticle scattering we examine two representative models of the pseudogap. Our goal is to understand how the interference patterns vary depending on whether the order parameter is in the p-p channel (superconductivity) or in the particle-hole channel.

A. Superconducting phase fluctuations

In this scenario the pseudogap state is viewed as a phase-disordered d -wave superconductor.¹ There exist several theoretical frameworks to describe such a state of electronic matter^{2,3,12,13,14} all sharing a common feature that the underlying order is in the pairing channel. Here we focus on the “QED₃” theory^{3,15} but it is easy to see that other approaches will yield similar general outcomes for the FT-STs patterns.

In the QED₃ theory, the phase of the superconducting order parameter is disordered by vortex-antivortex excitations that are encoded in a U(1) gauge field minimally coupled to the nodal fermions. At T_c , vortex-antivortex pairs unbind through the Kosterlitz-Thouless transition and cause a loss of phase coherence at long distances. The resulting pseudogap state is described by nodal fermions that are strongly interacting, the interaction mediated by the massless U(1) gauge field. The fermionic Green’s function in Nambu space¹⁵ is given by

$$G^0(\mathbf{k}, i\omega) = \lambda^{-\eta} \frac{i\omega + \epsilon_{\mathbf{k}}\sigma_3}{[\omega^2 + \epsilon_{\mathbf{k}}^2 + \Delta_{\mathbf{k}}^2]^{1-\eta/2}}, \quad (20)$$

where λ is a high energy cutoff and η is the anomalous dimension exponent which encodes the dressing of the nodal quasiparticles by the gauge field fluctuations. General requirements of causality and unitarity dictate that $\eta \geq 0$; however the exact value of the anomalous dimension is still under debate.^{15,29,30,31} Most believe that η is a small positive number. Here we sidestep these issues by treating η as a free parameter. We show that the FT-STs patterns are insensitive to its exact value.

The similarity between QED₃ propagator (20) and that of the d SC state suggests that the interference patterns obtained in this model will resemble those in the d SC state. We study the FT-STs patterns within the same set of approximations adopted for the d SC state, i.e. we evaluate $\Lambda(\mathbf{q}, \omega)$ and consider its real part. In addition, we note that the absence of the off-diagonal part in the QED₃ propagator (which reflects lack of long range superconducting order in the pseudogap state) implies that the $\Delta_+ \Delta_-$ term in $\Lambda(\mathbf{q}, \omega)$ will automatically vanish, irrespective of the type of scattering. Numerical evaluations of $\Lambda(\mathbf{q}, \omega)$ are carried out using the fast Fourier transform technique described above and the results are given in Fig. (6). As expected based on our general argument the QED₃ interference patterns are similar to those obtained for the d SC state. Peaks occur at the same points in the Brillouin zone and the anomalous

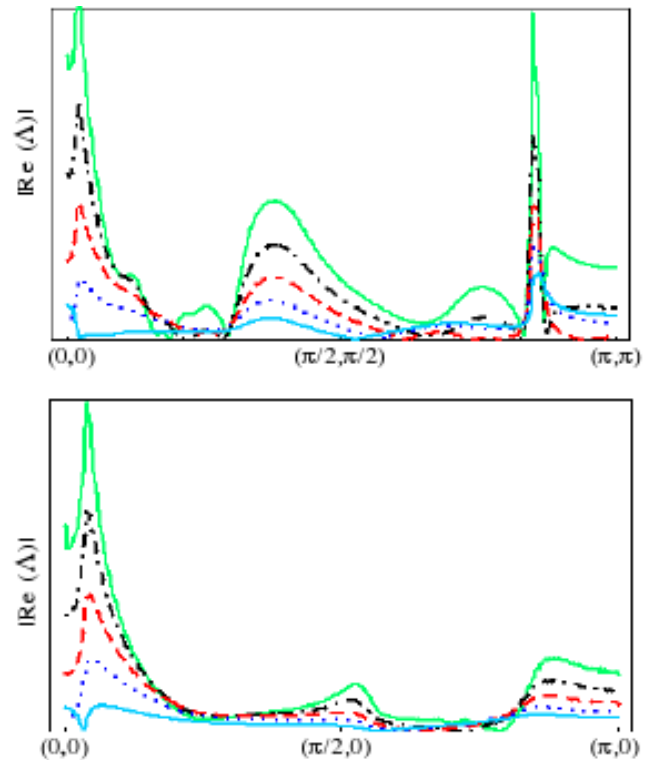


FIG. 6: The interference patterns within the QED₃ scenario with the anomalous dimension exponent $\eta = 0, 0.1, 0.2, 0.3$ and 0.4 , $\omega = 0.45\Delta_0$ and all other parameters as in Fig. (1). The upper panel displays a cut along the (π, π) direction of the Brillouin zone and the bottom plot is a cut along the $(\pi, 0)$ direction. In both panels, the solid, dashed-dotted, dashed, dotted and solid lines correspond to $\eta = 0, \dots, 0.4$ respectively.

dimension η causes some suppression of the sharp singularities.

This similarity can also be understood by performing the nodal approximation for the QED₃ propagators, which is done in appendix A. This treatment shows that the coherence factors produce the same angular dependence along the elliptic contour as in the d SC state, but the square root singularity is replaced by a weaker $1/(z^2 - 1)^{1/2-\eta}$ singularity, where $z = \omega/|\tilde{\mathbf{q}}|$ as before. Thus, the QED₃ and d SC patterns will be qualitatively similar as long as $0 \leq \eta < \frac{1}{2}$, which is exactly the range of values where we expect η to lie based on general considerations.

B. Competing orders

As an example of a model with competing orders we choose the d -density wave (DDW) theory.⁶ In this model, an order parameter of circulating currents with d -wave symmetry competes with superconductivity and dominates the pseudogap phase. The order parameter is in the particle-hole channel and connects excitations with

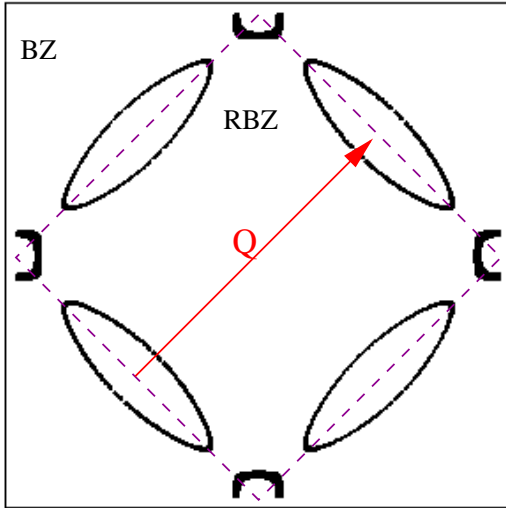


FIG. 7: The contour of constant energy for $\omega = 0.3D_0$ in the DDW model with $\mu = -t$, $D_0 = 0.1t$ and $t' = -0.3t$. The dashed line encloses the reduced Brillouin zone (RBZ) and \mathbf{Q} is the DDW vector. Note the electron pockets in the vicinity of $(\pm\pi, 0)$ and $(0, \pm\pi)$.

momentum difference of $\mathbf{Q} = (\pi, \pi)$ (see Fig. (7)). The Green's function is conveniently written in the basis of $\psi_{\mathbf{k}}^\dagger = (c_{\mathbf{k}}^\dagger, c_{\mathbf{k}+\mathbf{Q}}^\dagger)$,

$$G^0(\mathbf{k}, i\omega) = [(i\omega - \epsilon'_{\mathbf{k}}) - \epsilon''_{\mathbf{k}}\sigma_3 - D_{\mathbf{k}}\sigma_2]^{-1}, \quad (21)$$

with $\epsilon'_{\mathbf{k}} = \frac{1}{2}(\epsilon_{\mathbf{k}} + \epsilon_{\mathbf{k}+\mathbf{Q}})$, $\epsilon''_{\mathbf{k}} = \frac{1}{2}(\epsilon_{\mathbf{k}} - \epsilon_{\mathbf{k}+\mathbf{Q}})$, and the DDW gap $D_{\mathbf{k}} = \frac{1}{2}D_0(\cos k_x - \cos k_y)$. In this model, the Born approximation for the density of states modulations is given by

$$\begin{aligned} \Lambda(\mathbf{q}, i\omega) &= \text{Tr} \sum_{\mathbf{k}}' [G^0(\mathbf{k}, i\omega)(1 + \sigma_1)G^0(\mathbf{k} - \mathbf{q}, i\omega)] \\ &= \frac{2}{L^2} \sum_{\mathbf{k}}' \frac{-\Omega_+\Omega_- + \epsilon''_+\epsilon''_- + D_+D_-}{(\Omega_+^2 + E_+^2)(\Omega_-^2 + E_-^2)}, \quad (22) \end{aligned}$$

where $i\Omega_{\mathbf{k}} = i\omega - \epsilon'_{\mathbf{k}}$ and the prime on the summation indicates restriction to the reduced Brillouin zone depicted in Fig. (7). Derivation of this simple form is given in Appendix C. It is also worth noting that Eq. (22), also used by us previously,¹⁶ agrees with that used by Bena *et al.*³² in the appropriate limit of Born scattering.

When the DDW gap is close to the Fermi energy, i.e., close to half filling, the low energy excitations exist only near the nodes of the DDW gap. In this case we can linearize the spectrum in the vicinity of the nodes and approximate: $\epsilon'_{\mathbf{k}} \rightarrow 0$, $\Omega_{\mathbf{k}} \rightarrow \omega$, $\epsilon''_{\mathbf{k}} \rightarrow v_F k_1$ and $D_{\mathbf{k}} \rightarrow v_{\Delta} k_2$, where k_1 and k_2 are defined in the same way as in the *dSC* state. The linearized form of Eq. (22) turns out to be the same as that of a *magnetic* scatterer in the *dSC* state given by Eq. (16). This implies that close to half filling, a charge impurity in the DDW model is similar to a magnetic impurity in the *dSC*. This behavior is due to

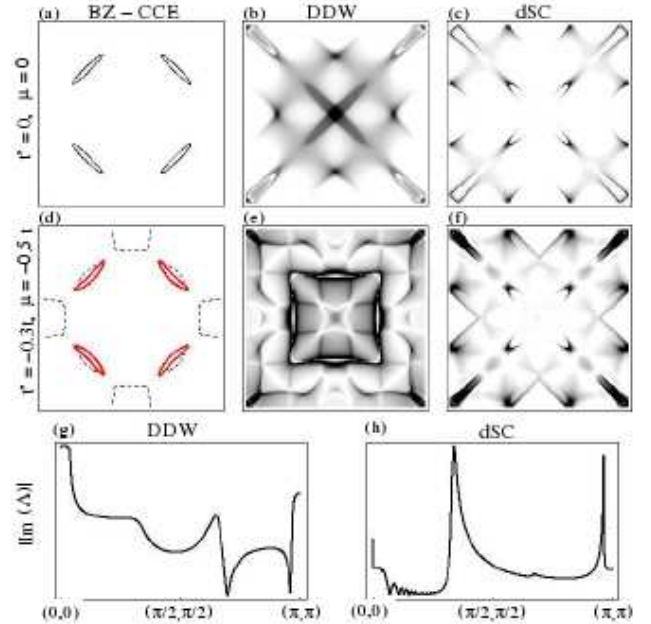


FIG. 8: Interference patterns in a DDW model of the pseudogap compared with a *dSC* model. Panels (a-c,g,h) show the results in the limit $\mu = 0$ and $t' = 0$. Panel (a) represents the contour of constant energy at $\omega = 0.5\Delta_0$. In this limit both models have the same CCE. Panels (b) and (c) show the calculated LDOS modulations in both models. These FT LDOS modulations differ from each other due to the different coherence factors as described in the text. These differences can also be seen in the one dimensional cut of the Brillouin zone along the (π, π) direction, shown in panels (g) and (h). Panel (d) shows the CCEs for the two different models when $t' = -0.3t$ and $\mu = -0.5t$. In this case the energy dispersions are different; the solid line is the banana shaped CCE of the *dSC* model while the dashed line represents the relevant CCE of the DDW model. The calculated FT-STs for this case are presented in panels (e) and (f). In all figures $\omega = 0.5\Delta_0$ and $\Delta_0 = D_0 = 0.5t$.

charge conservation in the DDW model, i.e., there is no BCS mixing to produce the angular dependent coherence factors of the *dSC* state.

The expression (22) can also be evaluated exactly numerically for all dopings, and we have done so with the same band structure as in the previous cases. The results are presented in Fig. (8) along with the results for a *dSC* with the same parameters.

The analytical and numerical calculations of the LDOS modulations in the DDW model show two principal differences between this theory and the BCS theory of the *dSC* state. First, the very different coherence factors lead to arc like patterns rather than peaks in the Brillouin zone. This feature cannot be altered by inclusion of higher order terms in the Born expansion (the *T*-matrix) due to the conservation of charge. The solution for the

T -matrix equation for the potential $V(1 + \sigma_1)$ gives

$$\hat{T}(\omega) = (1 + \sigma_1) \frac{V}{1 - g_0(\omega)V} \quad (23)$$

where $g_0(\omega) = \text{Tr} \sum_{\mathbf{k}} G^0(\mathbf{k}, \omega)$. This does not affect the matrix structure of the scattering vertex but merely adds some frequency dependence to it. The second difference is in the positions of features in the Brillouin zone. The positions are determined by the single particle dispersion, which in the DDW model is similar to that of a d SC state *only close to half filling* and in the absence of second nearest neighbor hopping t' . Upon choosing more realistic band parameters the CCE of this model develop electron pockets and deviate from those of the d SC state, as shown in Fig. (8-d). This is a result of the fact that the node of the DDW order parameter is *not* attached to the Fermi surface but to the $(\frac{\pi}{2}, \frac{\pi}{2})$ point in the Brillouin zone.

The patterns are most similar in the special case of $\mu = t' = 0$, i.e. exactly at half filling and with nearest neighbor hopping only. In this case the excitation spectra for DDW and d SC are identical. The coherence factors, however, are still different and give rise to qualitative differences in the FT-STs patterns. As shown in Fig. (8) away from this unphysical limit the patterns diverge even more and it should be straightforward to distinguish between them experimentally. This conclusion is independent of whether the superconducting state has coexisting DDW order or not. This is due to the fact that the FT LDOS spectrum in the mixed state is very similar to that of a pure d SC as was shown by Bena *et al.*³²

Our conclusions regarding the pure DDW state generally agree with those of Ref. 32, based on more detailed considerations within the T -matrix approach. In particular our original finding,¹⁶ that the FT-STs patterns in DDW and d SC states are qualitatively different, seems to emerge independently of details of the band structure and the scattering mechanism. We argued above that such differences are even more generic and will allow for discrimination between p-h and pairing origin of the underlying electron order in the pseudogap state.

C. Relation to experimental data

Recently, two groups succeeded in obtaining the FT-STs data in the pseudogap state of two different cuprate superconductors. Vershinin *et al.*³³ focused on the $T > T_c$ region in weakly underdoped samples of $\text{Bi}_2\text{Sr}_2\text{CaCu}_2\text{O}_{8+\delta}$ (BiSCCO), while Hanaguri *et al.*³⁴ studied lightly doped (non-superconducting) single crystals of $\text{Ca}_{2-x}\text{Na}_x\text{CuO}_2\text{Cl}_2$ (Na-CCOC) at low temperatures. In both cases no dispersive features could be identified. Instead, non-dispersive patterns with periodicity close to 4 lattice spacings have been reported in both experiments and interpreted as evidence for underlying static charge ordering. Precise nature of this or-

dering phenomenon is unclear at present and two scenarios involving a hole Wigner crystal³⁵ and a pair density wave^{36,37} have been proposed.

Absence of the quasiparticle interference patterns in Refs. 33,34 implies that the methods described in this work are not directly applicable to these experiments. A more promising in this respect is the recent experiment of McElroy *et al.*³⁸, which identifies ‘zero temperature pseudogap’ spectra in nominally superconducting samples of BiSCCO at low temperatures. Such ZTPG spectra coexist with the more conventional superconducting spectra and form characteristic nanoscale patchwork of interconnected regions. In strongly underdoped BiSCCO regions exhibiting ZTPG almost completely dominate the field of view. The interesting aspect of this data is that at low energies these ZTPG regions exhibit FT-STs interference patterns that look just like those observed deep in the superconducting state. At higher energy, however, non-dispersive peaks with periodicity close to 4 lattice spacing are observed in these same regions. These observations indicate that (i) the low energy quasiparticles in the ZTPG regions are of superconducting Nambu-Gorkov variety, and (ii) there exists an intimate relationship between the superconducting order and the new ordering phenomenon these materials.

An interesting question arises as to why are the dispersive peaks absent in the patterns observed in the pseudogap state. One possibility is that there are simply no sufficiently coherent quasiparticles that could form the interference patterns (such as in the QED₃ theory with $\eta > \frac{1}{2}$). Another possibility is that the patterns are present but have not been so far detected. It is entirely possible that in the BiSCCO experiment³³ done at $T \sim 100\text{K}$ delicate interference patterns are washed out by thermal broadening. The Na-CCOC experiment,³⁴ on the other hand, is done at $T \sim 0.1\text{K}$ and thermal smearing cannot be invoked. In this case it is interesting to note that no dispersive patterns have been observed in this material even in the superconducting state at higher doping. These considerations thus raise hopes that the interference patterns may be observed in future experiments and could help determine the nature of the pseudogap state in cuprates.

IV. CONCLUSIONS

We have shown that the quasiparticle interference patterns seen in the FT-STs experiments reveal signatures of both the quasiparticle dispersion and, through their sensitivity to the quasiparticle quantum phases, the *nature of the underlying electronic order* in the system. In particular, the quasiparticle phase determines the coherence factors, which then determine the basic characteristic features of the interference patterns. We have demonstrated, by general arguments and detailed calculations within two relevant models, that the superconducting order alone produces patterns consistent with the existing

experimental data. In particular, order of another type (such as DDW) yields *qualitatively different* patterns, even if the quasiparticle excitation spectrum is identical to the d SC.

The above feature is of key importance since it is in general difficult to model the details of FT-STS patterns, even in the well understood d SC state. This difficulty presumably arises from the complexities of the scattering processes which in realistic materials are likely caused by several distinct mechanisms and must be modeled as a combination of magnetic, non-magnetic and pairing potentials. In addition the matrix elements for the tunneling between the sample and the STS tip, ignored in most theoretical treatments, are likely to affect the patterns.

Despite these complexities, the FT-STS carries a wealth of useful information. Sensitivity of the interference patterns to the type of ordering implies that even though we might not be able to model their every detail in a particular state, we are assured that *the patterns will change* as the material crosses a phase boundary to a state characterized by a different electronic order.

Based on this insight we have proposed a test for the nature of the pseudogap phase in cuprates using FT-STS. The phase boundary in this case is $T_c(x)$, i.e. the superconducting critical temperature as a function of hole doping x . If the pseudogap is due to fluctuating SC order, then the FT-STS patterns above T_c should remain qualitatively the same as those below T_c . If, on the other hand, the pseudogap is due to an order parameter in the particle-hole channel, such as SDW, CDW or DDW, the patterns above T_c should be *qualitatively different*, due to their different coherence factors.

Although we focused here on one example of a particle-hole order parameter, the arguments presented above are general and can be applied to distinguish any such order from superconductivity. In addition, DDW order is perhaps the most germane to our argument since for specially selected parameters the excitation spectrum is the same as in the d SC. We have demonstrated that even in this special case the FT-STS patterns exhibit qualitative differences and should be easily distinguishable from the d SC. This is a result of the quasiparticle charge non-conservation in the superconductor which manifests itself

in the coherence factors of the FT-STS spectra. Other types of p-h order, such as SDW and CDW, will generally have very different excitation spectra, trivially implying different interference patterns.

By probing the interference patterns below and above $T_c(x)$, future FT-STS experiments should be able to unambiguously discriminate between the remnants of the superconducting order and an order in the particle-hole channel, thus settling one of the key puzzles in the high- T_c superconductivity.

Acknowledgments — The authors are indebted to J.C. Davis, T.P. Davis, V.P. Gusynin, J. Hoffman, A. Iyengar, D.-H. Lee, S. Sachdev, D.E. Sheehy, O. Vafek, Z. Tešanović and A. Yazdani for discussions and correspondence. This work was supported by NSERC, CIAR, the A.P. Sloan Foundation and partly by the NSF under grant No. PHY99-07949 (preprint NSF-KITP-04-11). One of the authors (M.F.) wishes to acknowledge the hospitality of the Aspen Center for Physics, where part of the work was performed and many stimulating discussions took place.

APPENDIX A: LINEARIZED APPROXIMATION

1. Non-magnetic scattering

Let us first consider the density of states modulations resulting from scattering within the same node in the linearized approximation given in Eq. (13). The solution, Eq. (14), can be found by “combining the denominators” using the Feynman parameterization.²⁸ This is based on the formula

$$\frac{1}{A^\alpha B^\beta} = \frac{\Gamma(\alpha + \beta)}{\Gamma(\alpha)\Gamma(\beta)} \int_0^1 dx \frac{x^{\alpha-1}(1-x)^{\beta-1}}{[xA + (1-x)B]^{\alpha+\beta}}, \quad (\text{A1})$$

where $\Gamma(z)$ is the Gamma function and the identity is valid for any positive A, B, α, β . Applying this to Eq. (13) with $\alpha = \beta = 1$ and performing a shift in the integration variable $\mathbf{k} \rightarrow \mathbf{k} + (1 - 2x)\tilde{\mathbf{q}}$ yields

$$\Lambda_{\text{lin}}(\mathbf{q}, i\omega) = \frac{1}{v_F v_\Delta} \int_0^1 dx \int \frac{d^2 k}{(2\pi)^2} \frac{-\omega^2 + (k_1^2 - k_2^2) - 4x(1-x)(\tilde{q}_1^2 - \tilde{q}_2^2)}{[\omega^2 + \mathbf{k}^2 + 4x(1-x)\tilde{\mathbf{q}}^2]^2}. \quad (\text{A2})$$

The $k_1^2 - k_2^2$ term vanishes in the angular integration and the radial integral is convergent. After performing the integration over momentum we get

$$\Lambda_{\text{lin}}(\mathbf{q}, i\omega) = \frac{1}{4\pi v_F v_\Delta} \int_0^1 dx \frac{-\omega^2 - 4x(1-x)(\tilde{q}_1^2 - \tilde{q}_2^2)}{\omega^2 + 4x(1-x)\tilde{\mathbf{q}}^2} \quad (\text{A3})$$

and the solution quoted in the text follows by performing the x integration and Wick rotating the frequency $i\omega \rightarrow \omega$ to get the retarded quantity.

Now consider a scattering process between two antipodal nodes, spanned by the vector \mathbf{Q} (shown in Fig. (2)) connecting the nodes along the (π, π) direction (the length of \mathbf{Q} varies with the doping). The linearized form of Λ is

similar to Eq. (14) with some signs inverted due to the different directions of v_F and v_Δ near the two nodes

$$\begin{aligned}\Lambda_{\text{lin}}(\mathbf{q} + \mathbf{Q}, i\omega) &= \frac{1}{v_F v_\Delta} \int \frac{d^2 k}{(2\pi)^2} \frac{-\omega^2 - (k_1^2 - k_2^2) + (\tilde{q}_1^2 - \tilde{q}_2^2)}{[\omega^2 + (\mathbf{k} - \tilde{\mathbf{q}})^2][\omega^2 + (\mathbf{k} + \tilde{\mathbf{q}})^2]} \\ &= \frac{1}{4\pi v_F v_\Delta} \int_0^1 dx \frac{-\omega^2 + 4x(1-x)(\tilde{q}_1^2 - \tilde{q}_2^2)}{\omega^2 + 4x(1-x)\tilde{\mathbf{q}}^2},\end{aligned}\quad (\text{A4})$$

where in the last line we have introduced the Feynman parameter x and performed the momentum integral. The result is given by Eq. (14) with the angular factor replaced by $\tilde{q}_1^2/\tilde{q}^2$. This 90° rotation of the angular factor causes the high intensity regions to be two points on the elliptic contour in the direction parallel to the vector \mathbf{Q} as shown in Fig. (3b). This is a deviation with respect to the octet model. Instead of the vectors \mathbf{q}_3 and \mathbf{q}_4 connecting the edges of the antipodal CCE bananas we obtain $\tilde{\mathbf{q}}_3 \approx \mathbf{q}_3$ at the points $\mathbf{Q} \pm \frac{2\omega}{v_F} \hat{q}_1$. The octet vector \mathbf{q}_4 is close to the point where the angular coherence factor vanishes and hence appears as an end of a line rather than a peak.

In the two cases above we have scaled the momenta k_1 and k_2 by v_F and v_Δ respectively to achieve radial symmetry. This convenient scaling can not be applied to the case of adjacent node scattering. For generic anisotropy one then obtains more complicated expressions which cannot be evaluated in a closed form. To keep things simple we treat this process in the limit of isotropic velocity $v_F = v_\Delta \equiv v$. If we denote by \mathbf{Q}' the vector that connects two adjacent nodes we have

$$\Lambda_{\text{lin}}(\mathbf{q} + \mathbf{Q}', i\omega) = \frac{1}{v^2} \int \frac{d^2 k}{(2\pi)^2} \frac{-\omega^2}{[\omega^2 + (\mathbf{k} - \tilde{\mathbf{q}})^2][\omega^2 + (\mathbf{k} + \tilde{\mathbf{q}})^2]}, \quad (\text{A5})$$

where we have omitted terms that are odd functions of ω . These would cancel later, when taking the appropriate components of Λ according to the prescription in Eq. (10). The solution is given by

$$\begin{aligned}\Lambda_{\text{lin}}(\mathbf{q}, \omega) &= \frac{1}{4\pi v^2} \left(\frac{\omega}{\tilde{q}}\right)^2 \mathcal{S}\left(\frac{\omega}{\tilde{q}}\right), \\ \mathcal{S}(z) &= \frac{1}{\sqrt{z^2 - 1}} \arctan \frac{1}{\sqrt{z^2 - 1}}.\end{aligned}\quad (\text{A6})$$

There is no angular dependence and the resulting Λ is just a uniform contour, as shown in Fig. (3d). More detailed considerations indicate that restoring the anisotropy would introduce a four-fold modulation of the intensity along the contour.

2. Magnetic scattering

The inter-nodal magnetic scattering can be calculated in a similar way for a magnetic point like impurity, where the only difference is the sign in front of the $\Delta_+ \Delta_-$ term in Eq. (12). This leads to the linearized form in Eq. (16) from which it can be readily seen that no angular dependent coherence factors emerge in this case. The solution, Eq. (17) is obtained by following the same steps as in the previous subsection. For antipodal nodes the result is the same as for the intra-nodal magnetic scattering, Eq. (12), where there is no angular dependence. However, when considering the case of scattering between adjacent nodes, the magnetic scattering exhibits angu-

lar dependence that generates peaks close to the octet model vectors $\mathbf{q}_1, \mathbf{q}_5$ and $\mathbf{q}_{2,6}$ even in the isotropic limit. The solution for this case is given by:

$$\Lambda_{\text{lin}}^{\text{mag}}(\mathbf{q}, \omega) = \frac{1}{4\pi v^2} \left(\frac{\tilde{q}_1 \tilde{q}_2 + \omega^2}{\tilde{q}^2}\right) \mathcal{S}\left(\frac{\omega}{\tilde{q}}\right), \quad (\text{A7})$$

where $\mathcal{S}(z)$ is defined in Eq. (A6) and the factor of $\tilde{q}_1 \tilde{q}_2 / \tilde{q}^2$ is responsible for four peaks along the contour, near the octet vectors $\mathbf{q}_1, \mathbf{q}_5$, and $\mathbf{q}_{2,6}$ as shown in Fig. (3c).

The above analysis suggests that a combination of non-magnetic and magnetic scattering is needed to produce sharp peaks at all the octet vectors. The exception is \mathbf{q}_4 which marks the end of a line produced by Eq. (A4). The linearized approximation results are given in Fig. (3). In panel (e) we have also combined together the results for non-magnetic scattering to cover the entire Brillouin zone. For adjacent node scattering we use magnetic results which show the four-fold modulation expected for the anisotropic case.

3. QED₃

The nodal approximation is also useful for the case of propagators with anomalous dimensions, as in the case of QED₃. Let us consider the intra-nodal scattering processes within the QED₃ framework. We use the same Feynman parameterization as before, where this time $\alpha = \beta = 1 - \eta/2$. This leads to the following integral

$$\begin{aligned}
\Lambda_\eta(\mathbf{q}, i\omega) &= \frac{1}{v_F v_\Delta} \int \frac{d^2 k}{(2\pi)^2} \frac{(i\omega + k_1 + \tilde{q}_1)(i\omega + k_1 - \tilde{q}_1)}{[\omega^2 + (\mathbf{k} + \tilde{\mathbf{q}})^2]^{1-\eta/2} [\omega^2 + (\mathbf{k} - \tilde{\mathbf{q}})^2]^{1-\eta/2}} \\
&= \frac{1}{v_F v_\Delta} \frac{\Gamma(2-\eta)}{(\Gamma(1-\eta/2))^2} \int_0^1 dx [x(1-x)]^{-\eta/2} \int \frac{d^2 k}{(2\pi)^2} \frac{-\omega^2 + k_1^2 - 4x(1-x)\tilde{q}_1^2}{[\omega^2 + \mathbf{k}^2 + 4x(1-x)\tilde{\mathbf{q}}^2]^{2-\eta}}
\end{aligned} \quad (\text{A8})$$

where the last line was obtained by the variable shift $\mathbf{k} \rightarrow \mathbf{k} - (2x-1)\tilde{\mathbf{q}}$. We can now evaluate the momentum integral by first performing the angular integration and then the radial part with a momentum cutoff λ . We obtain

$$\begin{aligned}
\int \frac{d^2 k}{(2\pi)^2} \dots &= \frac{1}{4\pi(1-\eta)} \left(\frac{\omega^2 + 4x(1-x)\tilde{q}_1^2}{[\omega^2 + 4x(1-x)\tilde{\mathbf{q}}^2]^{1-\eta}} + \frac{1}{2\eta} [\lambda^{2\eta} - (\omega^2 + 4x(1-x)\tilde{\mathbf{q}}^2)^\eta] \right) \\
&= \frac{1}{4\pi(1-\eta)} \left([\omega^2 + 4x(1-x)\tilde{\mathbf{q}}^2]^\eta - \frac{4x(1-x)\tilde{q}_2^2}{[\omega^2 + 4x(1-x)\tilde{\mathbf{q}}^2]^{1-\eta}} + \frac{1}{2\eta} [\lambda^{2\eta} - (\omega^2 - 4x(1-x)\tilde{\mathbf{q}}^2)^\eta] \right),
\end{aligned} \quad (\text{A9})$$

where only the middle term is divergent. We therefore proceed considering the divergent term only,

$$\Lambda_\eta(\mathbf{q}, i\omega)|_{div} = \frac{1}{(1-\eta)} \frac{1}{4\pi v_F v_\Delta} \frac{\Gamma(2-\eta)}{(\Gamma(1-\eta/2))^2} \int_0^1 dx [x(1-x)]^{-\eta/2} \frac{4x(1-x)\tilde{q}_2^2}{[\omega^2 + 4x(1-x)\tilde{\mathbf{q}}^2]^{1-\eta}}. \quad (\text{A10})$$

By performing the Wick rotation and using $z^2 = \omega^2/\tilde{\mathbf{q}}^2$ we find

$$\Lambda_\eta(\mathbf{q}, \omega) \propto \left(\frac{\tilde{q}_2}{\tilde{\mathbf{q}}} \right)^2 \int_0^1 dx \frac{[x(1-x)]^{1-\eta/2}}{[x(1-x) - (\frac{z}{2})^2]^{1-\eta}}. \quad (\text{A11})$$

The angular dependence of Λ along the elliptic contour is already explicit in the above expression and is the same as in the d SC intra-nodal scattering case. Unfortunately, the Feynman parameter integration can not be performed analytically for all values of z . For the case of $z < 1$ Eq. A11 can be evaluated using hypergeometric functions but no such expansion exists for $z \geq 1$. We therefore choose to analyze the integral and find its degree of divergence. First note that the denominator is divergent whenever $z^2 = 4x(1-x)$. For any given value of z^2 this leads to two singularities at $x/2 = -1 \pm \sqrt{1-z^2}$. However, since η is positive and smaller than 1, the singularities are integrable unless they overlap. Therefore, the integral is only divergent when $z^2 = 1$. In order to find the degree of divergence we shift the integration variable $x \rightarrow x - 1/2$ and denote $b = (1-z^2)/4$. The x integral, $I(z)$, is given by

$$\begin{aligned}
I(z) &= 2 \int_0^{\frac{1}{2}} dx \frac{(\frac{1}{4} - x^2)^{1-\eta/2}}{(b-x^2)^{1-\eta}} \\
&= 2 \left(\frac{1}{b} \right)^{1-\eta} \int_0^{\frac{1}{2}} dx \frac{(\frac{1}{4} - x^2)^{1-\eta/2}}{[1 - (\frac{x}{\sqrt{b}})^2]^{1-\eta}}.
\end{aligned} \quad (\text{A12})$$

We can now define a new integration variable $y = \frac{x}{\sqrt{b}}$ and write

$$I(z) = 2 \left(\frac{1}{b} \right)^{\frac{1}{2}-\eta} \int_0^{\frac{1}{2\sqrt{b}}} dy \frac{(\frac{1}{4} - by^2)^{1-\eta/2}}{(1-y^2)^{1-\eta}}.$$

The remaining integral is convergent in the limit $b \rightarrow 0$. The integration thus can be performed on $[0, \infty)$ and

the singularity, given by the prefactor, is of the order of $1/(1-z^2)^{1/2-\eta}$, as stated in the text.

APPENDIX B: GAP SUPPRESSION IN A d -WAVE SUPERCONDUCTOR

In order to take into account the gap modulations in the sample we introduce a local perturbation which will be referred to as the *gap suppression*. We start with a lattice model where both the hopping amplitudes t, t' and the gap function Δ_{ij} are defined on the bonds. We assume that $\Delta_{ij} = \pm\Delta_0$ on nearest neighbors and is zero everywhere else, with plus and minus sign corresponding to x and y oriented bonds respectively. On top of this uniform state we introduce a gap suppression $\delta\Delta(\mathbf{R})$ on four bonds around the point \mathbf{R} , as shown in Fig. (9). The distribution of these impurities is assumed to be a featureless function of \mathbf{R} . The gap modulation produces the following perturbation:

$$\begin{aligned}
\delta\mathcal{H} &= \sum_{\langle \mathbf{R}, \mathbf{R}' \rangle} [\delta\Delta(\mathbf{R}) c_{\mathbf{R}}^\dagger c_{\mathbf{R}'}^\dagger \chi(\mathbf{R} - \mathbf{R}') + \text{h.c.}] \\
&= \sum_{\mathbf{p}, \mathbf{k}} [\delta\Delta_{\mathbf{p}} \chi_{\mathbf{k}} c_{\mathbf{p}}^\dagger c_{\mathbf{k}}^\dagger + \text{h.c.}],
\end{aligned} \quad (\text{B1})$$

where $\langle \dots \rangle$ denotes the nearest neighbors on the lattice, $\chi(\mathbf{R} - \mathbf{R}')$ is the sign of the perturbation, depending on the bond orientation and $\chi_{\mathbf{k}} = \cos k_x - \cos k_y$. To leading order, this potential leads to the following LDOS modulation

$$\delta n(\mathbf{q}, \omega) = -\frac{1}{\pi} |\delta\Delta_{\mathbf{q}}| \text{Im} [\Lambda_{11}(\mathbf{q}, \omega) + \Lambda_{22}(\mathbf{q}, -\omega)], \quad (\text{B2})$$

with

$$\Lambda(\mathbf{q}, \omega) = \sum_{\mathbf{k}} G^0(\mathbf{k}, \omega) \chi_{\mathbf{k}} \sigma_1 G^0(\mathbf{k} - \mathbf{q}, \omega). \quad (\text{B3})$$

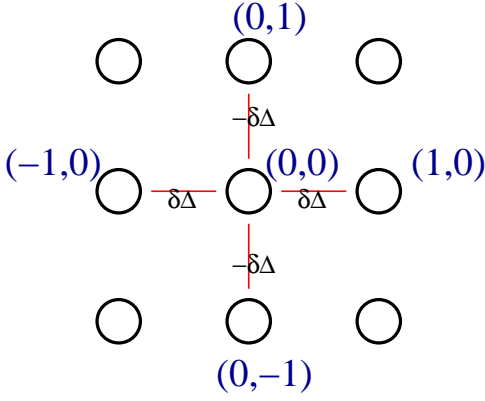


FIG. 9: The gap modulation local perturbation around the lattice point $\mathbf{R} = (0, 0)$.

Note that the perturbation $\chi_{\mathbf{k}}\sigma_1$ is only a function of one momentum index, conjugate to the relative coordinate $\mathbf{R} - \mathbf{R}'$.

One can go further and find the T -matrix for a combined local potential of a charge impurity and a gap suppression. For simplicity, we assume that the same dilute array of impurities is responsible for both perturbations and treat the single impurity at the origin in the T -matrix approach. For the combined potential $V_{\mathbf{k}\mathbf{k}'} = V\sigma_3 + \delta\Delta\chi_{\mathbf{k}}\sigma_1$ the T -matrix equation (6) can be solved using the ansatz

$$\hat{T}_{\mathbf{k}\mathbf{k}'}(\omega) = T_0(\omega)\sigma_0 + T_3(\omega)\sigma_3 + T_1(\omega)\chi_{\mathbf{k}}\sigma_1. \quad (\text{B4})$$

The frequency dependent coefficients are given by:

$$\begin{aligned} T_0(\omega) &= \frac{g_0(\omega)V^2}{A(\omega)}, \\ T_3(\omega) &= V\frac{1 - g_1(\omega)V}{A(\omega)}, \\ T_1(\omega) &= \delta\Delta\frac{1 - g_1(\omega)V}{A(\omega)}, \end{aligned}$$

with

$$A(\omega) \equiv [1 - g_1(\omega)V]^2 - [g_0(\omega)V]^2 - g_d(\omega)\delta\Delta[1 - g_1(\omega)V]. \quad (\text{B5})$$

$g_i(\omega)$ are functions of the frequency, resulting from the momentum integration of different parts of the unperturbed Green's function:

$$\begin{aligned} g_0(\omega) &= \sum_{\mathbf{k}} \frac{\omega}{\omega^2 - E_{\mathbf{k}}^2} \\ g_1(\omega) &= \sum_{\mathbf{k}} \frac{\epsilon_{\mathbf{k}}}{\omega^2 - E_{\mathbf{k}}^2} \\ g_d(\omega) &= \sum_{\mathbf{k}} \frac{\chi_{\mathbf{k}}\Delta_{\mathbf{k}}}{\omega^2 - E_{\mathbf{k}}^2}. \end{aligned} \quad (\text{B6})$$

This T -matrix has a resonant structure in frequency, similar to that found by Balatsky *et al.* for the case of a

charge impurity.²⁴ However, we are interested in a particular regime of frequencies and scattering strength which may not coincide with the resonance. The advantage of this formalism in this case is the mixture of different scattering components and the finite imaginary part of the T -matrix.

APPENDIX C: QUASIPARTICLE SCATTERING IN D-DENSITY WAVE MODEL

In order to calculate $\Lambda(\mathbf{q}, \omega)$ in the DDW model one has to carefully define quantities in the reduced Brillouin zone (RBZ) shown in Fig. (7). Our starting point will be the unperturbed DDW Hamiltonian⁶

$$\begin{aligned} \mathcal{H} &= \sum_{\mathbf{k}} [\epsilon_{\mathbf{k}} a_{\mathbf{k}}^\dagger a_{\mathbf{k}} + iD_{\mathbf{k}} a_{\mathbf{k}}^\dagger a_{\mathbf{k}+\mathbf{Q}} - iD_{\mathbf{k}} a_{\mathbf{k}+\mathbf{Q}}^\dagger a_{\mathbf{k}}] \\ &\equiv \sum_{\mathbf{k}}' \psi_{\mathbf{k}}^\dagger \mathcal{H}_{\mathbf{k}} \psi_{\mathbf{k}} \end{aligned} \quad (\text{C1})$$

where $a_{\mathbf{k}}$ are the electron operators, the prime denotes a sum over RBZ wave vectors and $D_{\mathbf{k}}$ is the DDW order parameter. We have defined $\psi_{\mathbf{k}}^\dagger = (c_{\mathbf{k}}^\dagger, d_{\mathbf{k}}^\dagger)$ such that $c_{\mathbf{k}}$ is the usual electron annihilation operator, $a_{\mathbf{k}}$ when \mathbf{k} is in the reduced Brillouin zone and $d_{\mathbf{k}+\mathbf{Q}}$ is the usual electron annihilation operator when \mathbf{k} is outside of the RBZ (and $\mathbf{k} + \mathbf{Q} \in \text{RBZ}$). The operators c and d are defined only in the RBZ and therefore their labels should be understood modulo $\mathbf{Q} = (\pi, \pi)$. In what follows we maintain the labels of c , d and ψ explicitly in the RBZ. In this basis the matrix $\mathcal{H}_{\mathbf{k}}$ is given by:

$$\mathcal{H}_{\mathbf{k}} = \begin{pmatrix} \epsilon_{\mathbf{k}} & -iD_{\mathbf{k}} \\ iD_{\mathbf{k}} & \epsilon_{\mathbf{k}+\mathbf{Q}} \end{pmatrix} \quad (\text{C2})$$

For simplicity we consider point scattering described by the Hamiltonian

$$\begin{aligned} \delta\mathcal{H} &= \sum_{\mathbf{r}} V\delta(\mathbf{r})a_{\mathbf{r}}^\dagger a_{\mathbf{r}} = V \sum_{\mathbf{p}, \mathbf{p}'} a_{\mathbf{p}}^\dagger a_{\mathbf{p}'} \\ &= V \sum_{\mathbf{p}, \mathbf{p}'}' \psi_{\mathbf{p}}^\dagger (1 + \sigma_1) \psi_{\mathbf{p}'}. \end{aligned} \quad (\text{C3})$$

The same conclusion can be derived for arbitrary weak potential.

In order to calculate the tunneling amplitude we use the interaction representation, where the DDW Hamiltonian \mathcal{H} represents the uniform system and $\delta\mathcal{H}$ is the interaction. We express the Green's function in terms of RBZ momenta and expand it to first order in the interaction. The single particle Green's function is given by

$$G(\mathbf{r}, \mathbf{r}'; t - t') = -i \frac{\langle T a_{\mathbf{r}}(t) a_{\mathbf{r}'}^\dagger(t') S(\infty, -\infty) \rangle}{\langle S(\infty, -\infty) \rangle} \quad (\text{C4})$$

where the S -matrix is responsible for the time evolution of operators by the interaction $\delta\mathcal{H}$, the angular brackets denote the vacuum expectation values and T is the

time ordering operator. We shall now focus on the equal point propagator $G(\mathbf{r}, \mathbf{r}; t - t')$ and consider its Fourier transform with respect to \mathbf{r}

$$\tilde{G}(\mathbf{q}; t - t') \equiv \int d\mathbf{r} e^{-i\mathbf{q}\cdot\mathbf{r}} G(\mathbf{r}, \mathbf{r}; t - t') = \frac{-i}{\langle S(\infty, -\infty) \rangle} \sum_{\mathbf{k}} \langle T a_{\mathbf{k}}(t) a_{\mathbf{k}-\mathbf{q}}^\dagger(t') S(\infty, -\infty) \rangle. \quad (\text{C5})$$

The momentum indices are defined in the full Brillouin zone, where one of the following four cases may occur. Both \mathbf{k} and $\mathbf{k} - \mathbf{q}$ are in the RBZ, both are outside of the RBZ, $\mathbf{k} \in \text{RBZ}$ and $\mathbf{k} - \mathbf{q} \notin \text{RBZ}$ or $\mathbf{k} \notin \text{RBZ}$ and $\mathbf{k} - \mathbf{q} \in \text{RBZ}$. In the RBZ we can write this as

$$\begin{aligned} \tilde{G}(\mathbf{q}; t - t') &= \frac{-i}{\langle S(\infty, -\infty) \rangle} \sum_{\mathbf{k}}' \langle T \{ [c_{\mathbf{k}}(t) c_{\mathbf{k}-\mathbf{q}}^\dagger(t') + d_{\mathbf{k}}(t) d_{\mathbf{k}-\mathbf{q}}^\dagger(t')] \Theta(\mathbf{k} - \mathbf{q}) + \\ &\quad [c_{\mathbf{k}}(t) d_{\mathbf{k}-\mathbf{q}+\mathbf{Q}}^\dagger(t') + d_{\mathbf{k}}(t) c_{\mathbf{k}-\mathbf{q}+\mathbf{Q}}^\dagger(t')] \bar{\Theta}(\mathbf{k} - \mathbf{q}) \} S(\infty, -\infty) \rangle \\ &= \frac{-i}{\langle S(\infty, -\infty) \rangle} \text{Tr} \sum_{\mathbf{k}}' \langle T \{ \psi_{\mathbf{k}}(t) \psi_{\mathbf{k}-\mathbf{q}}^\dagger(t') \Theta(\mathbf{k} - \mathbf{q}) + \sigma_1 \psi_{\mathbf{k}}(t) \psi_{\mathbf{k}-\mathbf{q}+\mathbf{Q}}^\dagger(t') \bar{\Theta}(\mathbf{k} - \mathbf{q}) \} (t') S(\infty, -\infty) \rangle. \end{aligned} \quad (\text{C6})$$

where

$$\Theta(\mathbf{k}) = \begin{cases} 1, & \mathbf{k} \in \text{RBZ} \\ 0, & \mathbf{k} \notin \text{RBZ} \end{cases}, \quad \bar{\Theta}(\mathbf{k}) = 1 - \Theta(\mathbf{k}).$$

In the last line of (C6) we introduced the σ_1 Pauli matrix in the trace in order to implement the sum over off-diagonal elements of the 2×2 matrix $\psi_{\mathbf{k}} \psi_{\mathbf{k}-\mathbf{q}}^\dagger$.

We now include the perturbation in the S -matrix to first order, i.e., we approximate $S(\infty, -\infty) \approx 1 - i \int \delta \mathcal{H} dt$. Dropping the unperturbed part of the Fourier transformed Green's function we find the first order correction

$$\tilde{G}^{(1)}(\mathbf{q}; t - t') = -V \text{Tr} \sum_{\mathbf{kpp}'}' \int dt'' \langle T \{ \psi_{\mathbf{k}}(t) \psi_{\mathbf{k}-\mathbf{q}}^\dagger(t') \Theta(\mathbf{k} - \mathbf{q}) + \sigma_1 \psi_{\mathbf{k}}(t) \psi_{\mathbf{k}-\mathbf{q}+\mathbf{Q}}^\dagger(t') \bar{\Theta}(\mathbf{k} - \mathbf{q}) \} \psi_{\mathbf{p}}^\dagger(t'') (1 + \sigma_1) \psi_{\mathbf{p}}(t'') \rangle. \quad (\text{C7})$$

Performing Wick contractions and a time Fourier transform yields the quantity $\Lambda(\mathbf{q}, \omega)$, defined in the text:

$$\begin{aligned} \Lambda(\mathbf{q}, \omega) &= \frac{1}{V} \int dt e^{-i\omega(t-t')} G^{(1)}(\mathbf{q}; t - t') \\ &= \text{Tr} \sum_{\mathbf{k}}' \int dt'' dt e^{-i\omega(t-t')} [G^0(\mathbf{k}, t - t'') (1 + \sigma_1) G^0(\mathbf{k} - \mathbf{q}, t'' - t') \Theta(\mathbf{k} - \mathbf{q}) \\ &\quad + \sigma_1 G^0(\mathbf{k}, t - t'') (1 + \sigma_1) G^0(\mathbf{k} - \mathbf{q} + \mathbf{Q}, t'' - t') \bar{\Theta}(\mathbf{k} - \mathbf{q})] \\ &= \text{Tr} \sum_{\mathbf{k}}' [G^0(\mathbf{k}, \omega) (1 + \sigma_1) G^0(\mathbf{k} - \mathbf{q}, \omega) \Theta(\mathbf{k} - \mathbf{q}) + \sigma_1 G^0(\mathbf{k}, \omega) (1 + \sigma_1) G^0(\mathbf{k} - \mathbf{q} + \mathbf{Q}, \omega) \bar{\Theta}(\mathbf{k} - \mathbf{q})] \end{aligned} \quad (\text{C8})$$

where $G^0(\mathbf{k}, \omega)$ is the unperturbed DDW Green's function given in Eq. (21). The above expression can be simplified further. Let us concentrate on the second term when $\mathbf{k} - \mathbf{q} \notin \text{RBZ}$. If we now extend the definition of the Green's function to hold even when the argument is not in the RBZ (using the functional definitions of $\epsilon_{\mathbf{k}}$ and $D_{\mathbf{k}}$), we find that $G^0(\mathbf{k} + \mathbf{Q}, \omega) = \sigma_1 G^0(\mathbf{k}, \omega) \sigma_1$. Rewriting the second term we find:

$$\begin{aligned} \text{Tr} [\sigma_1 G^0(\mathbf{k}, \omega) (1 + \sigma_1) G^0(\mathbf{k} + \mathbf{q} + \mathbf{Q}, \omega)] &= \text{Tr} [\sigma_1 G^0(\mathbf{k}, \omega) (1 + \sigma_1) \sigma_1 G^0(\mathbf{k} + \mathbf{q}, \omega) \sigma_1] \\ &= \text{Tr} [G^0(\mathbf{k}, \omega) (1 + \sigma_1) G^0(\mathbf{k} + \mathbf{q}, \omega)]. \end{aligned} \quad (\text{C9})$$

Therefore

$$\Lambda(\mathbf{q}, \omega) = \sum_{\mathbf{k}}' \text{Tr} [G^0(\mathbf{k}, \omega) (1 + \sigma_1) G^0(\mathbf{k} + \mathbf{q}, \omega)], \quad (\text{C10})$$

where $\mathbf{k} + \mathbf{q}$ need not be in the RBZ.

¹ V.J. Emery and S.A. Kivelson, Nature **374**, 434 (1995).

² L. Balents, M.P.A. Fisher and C. Nayak, Phys. Rev. B **60**,

- 1654 (1999).
- ³ M. Franz and Z. Tešanović, Phys. Rev. Lett. **87**, 257003 (2001).
 - ⁴ S.C. Zhang, Science **275**, 1089 (1997).
 - ⁵ R. B. Laughlin, cond-mat/0209269.
 - ⁶ S. Chakravarty, R.B. Laughlin, D.K. Morr, and C. Nayak Phys. Rev. B **63**, 094503 (2001).
 - ⁷ T. Timusk and B.W. Statt, Rep. Prog. Phys. **62**, 61 (1999).
 - ⁸ M. Sutherland, D. G. Hawthorn, R. W. Hill, F. Ronning, S. Wakimoto, H. Zhang, C. Proust, E. Boaknin, C. Lupien, L. Taillefer, R. Liang, D. A. Bonn, W. N. Hardy, R. Gagnon, N. E. Hussey, T. Kimura, M. Nohara, and H. Takagi Phys. Rev. B **67**, 174520 (2003).
 - ⁹ T. Valla, A. V. Fedorov, P. D. Johnson, Q. Li, G. D. Gu, and N. Koshizuka Phys. Rev. Lett. **85**, 828 (2000).
 - ¹⁰ C.M. Varma, Phys. Rev. Lett. **83**, 3538 (1999).
 - ¹¹ M. Vojta, Y. Zhang, and S. Sachdev, Phys. Rev. B **62**, 6721 (2000).
 - ¹² M. Randeria, *Varenna Lectures* (cond-mat/9710223).
 - ¹³ M. Franz and A.J. Millis, Phys. Rev. B **58**, 14572 (1998).
 - ¹⁴ Q. Chen, K. Levin and I. Kosztin, Phys. Rev. B **63**, 184519 (2001).
 - ¹⁵ M. Franz, Z. Tešanović and O. Vafek, Phys. Rev. B **66**, 054535 (2002).
 - ¹⁶ T. Pereg-Barnea and M. Franz, Phys. Rev. B **68**, 180506(R) (2003).
 - ¹⁷ J. Hoffman, K. McElroy, D.-H. Lee, K.M Lang, H. Eisaki, S. Uchida, J.C. Davis, Science **297** 1148(2002).
 - ¹⁸ K. McElroy, R. W. Simmonds, J.E. Hoffman, D.-H. Lee, J. Orenstein, H. Eisaki, S. Uchida & J.C. Davis, Nature **422** 592(2003).
 - ¹⁹ C. Howald, H. Eisaki, N. Kaneko, M. Greven, and A. Kapitulnik, Phys. Rev. B **67**, 014533 (2003).
 - ²⁰ Q.-H. Wang and D.-H. Lee, Phys. Rev. B **67**, 020511(2003).
 - ²¹ L. Capriotti, D.J. Scalapino and R.D. Sedgewick, Phys. Rev. B **68**, 014508 (2003).
 - ²² A. Polkovnikov, S. Sachdev and M. Vojta, Physica C **388**, 19 (2003).
 - ²³ Lingyin Zhu, W. A. Atkinson, and P. J. Hirschfeld, Phys. Rev. B **69**, 060503 (2004).
 - ²⁴ A. V. Balatsky, M. I. Salkola, and A. Rosengren, Phys. Rev. B **51** 15547 (1995).
 - ²⁵ S. H. Pan, J. P. O'Neal, R. L. Badzey, C. Chamon, H. Ding, J. R. Engelbrecht, Z. Wang, H. Eisaki, S. Uchida, A. K. Gupta, K. -W. Ng, E. W. Hudson, K. M. Lang and J. C. Davis, Nature **413** 282 (2001).
 - ²⁶ Ziqiang Wang, Jan R. Engelbrecht, Shancai Wang, Hong Ding, and Shuheng Pan, Phys. Rev. B **65** 064509 (2002).
 - ²⁷ In the Born approximation the power spectrum is proportional to the modulus square of the potential, see for example Ref. 21.
 - ²⁸ See e.g. M. E. Peskin and D. V. Schroeder, *An Introduction to Quantum Field Theory*, Addison-Wesley 1995.
 - ²⁹ D.V. Khveshchenko, Phys. Rev. B **65**, 235111 (2002).
 - ³⁰ W. Rantner and X.-G. Wen, Phys. Rev. Lett. **86**, 3871 (2001).
 - ³¹ V.P. Gusynin, D.V. Khveshchenko and M. Reenders, Phys. Rev. B **67**, 115201 (2003).
 - ³² C. Bena, S. Chakravarty, J. Hu and C. Nayak, Phys. Rev. B **69**, 134517 (2004).
 - ³³ M. Vershinin, S. Misra, S. Ono, Y. Abe, Y. Ando, A. Yazdani, *Science* **303**, 1995 (2004).
 - ³⁴ T. Hanaguri, C. Lupien, Y. Koshaka, D.-H. Lee, M. Azuma, M. Takano, H. Takagi, J.C. Davis, *Nature* (to appear).
 - ³⁵ H.C. Fu, J.C. Davis, D.H. Lee, cond-mat/0403001.
 - ³⁶ H.D. Chen, O. Vafek, A. Yazdani, S.-C. Zhang, Phys. Rev. Lett. **93**, 187002 (2004).
 - ³⁷ Z. Tesanovic, Phys. Rev. Lett. **93**, 217004 (2004).
 - ³⁸ K. McElroy, D.-H. Lee, J.E. Hoffman, K.M. Lang, E.W. Hudson, H. Eisaki, S. Uchida, J. Lee, J.C. Davis, cond-mat/0404005.